# Directional Sensitivity of DAS and Its Effect on Rayleigh-Wave Tomography: A Case Study in Oxnard, California

Jiaqi Fang<sup>\*1</sup>, Yan Yang<sup>1</sup>, Zhichao Shen<sup>1</sup>, Ettore Biondi<sup>1</sup>, Xin Wang<sup>1,2</sup>, Ethan F. Williams<sup>1</sup>, Matthew W. Becker<sup>3</sup>, Dominic Eslamian<sup>3</sup>, and Zhongwen Zhan<sup>1</sup>

#### **Abstract**

Distributed acoustic sensing (DAS) provides dense arrays ideal for seismic tomography. However, DAS only records average axial strain change along the cable, which can complicate the interpretation of surface-wave observations. With a rectangular DAS array located in the City of Oxnard, California, we compare phase velocity dispersion at the same location illuminated by differently oriented virtual sources. The dispersion curves are consistent for colinear and noncolinear virtual sources, suggesting that surface-wave observations in most of the cross-correlations are dominated by Rayleigh waves. Our measurements confirm that colinear channel pairs provide higher Rayleigh-wave signal-to-noise ratio (SNR). For cross-correlations of noncolinear channel pairs, the travel time of each connecting ray path can still be obtained despite the lower SNR of Rayleigh wave signals. The inverted Rayleigh-wave dispersion map reveals an ancient river channel consistent with the local geologic map. Our results demonstrate the potential of DAS-based 2D surface-wave tomography without special treatment of directional sensitivity in areas where one type of wave is dominating or can be identified.

Cite this article as Fang, J., Y. Yang, Z. Shen, E. Biondi, X. Wang, E. F. Williams, M. W. Becker, D. Eslamian, and Z. Zhan (2022). Directional Sensitivity of DAS and Its Effect on Rayleigh-Wave Tomography: A Case Study in Oxnard, California, Seismol. Res. Lett. 94, 887–897, doi: 10.1785/0220220235.

**Supplemental Material** 

#### Introduction

The geology underneath a city is a significant consideration in evaluating and managing seismic risk (Borcherdt and Gibbs, 1976; Aki, 1993; Graves et al., 1998; Olsen et al., 2006). Scientists have put great effort toward obtaining accurate subsurface velocity images to probe highly variable underlying materials and localize fine-scale structures (Michael and Eberhart-Phillips, 1991). Various tomographic methods have been developed for this purpose, including surface-wave tomography (Shapiro et al., 2005; Nishida et al., 2009), eikonal tomography (Lin et al., 2013), full-waveform tomography (Lee et al., 2014), and machine learning-based tomography (Bianco et al., 2019). Surface-wave tomography with ambient noise interferometry is one of the simplest approaches for deriving subsurface velocity models by cross-correlating ambient noise between each station pair and extracting the Green's function along the ray path (Snieder, 2004; Shapiro et al., 2005). However, dense geophone arrays for high-resolution mapping require high maintenance costs, and their deployment in metropolitan areas is limited by space constraints.

Distributed acoustic sensing (DAS) provides a cost-effective solution to acquiring continuous high-resolution seismic observations by converting pre-existing fiber-optic cables into numerous recording channels effectively spaced every few meters (Zhan, 2020; Lindsey and Martin, 2021). A DAS interrogator

unit sends laser pulses down to the fiber and measures the phase change of backscattered light from natural heterogeneities along the fiber to infer the axial strain change (Lindsey *et al.*, 2020). Urban telecommunication cables can thus offer dense seismic data ideal for ambient noise imaging (Dou *et al.*, 2017; Ajo-Franklin *et al.*, 2019; Yang, Atterholt, *et al.*, 2022).

DAS can only record axial strain or strain rate in most cases, except for specialized cable layouts, such as helically wound fibers (Kuvshinov, 2016; Lim Chen Ning and Sava, 2018). For cable networks without advanced multidirectional design, DAS unavoidably has directional sensitivity to different kinds of seismic waves. Ambient noise tomography is commonly performed considering colinear channels, such that the resulting cross-correlation functions only have surface waves of the Rayleigh type (Yang, Atterholt, et al., 2022). In this scenario, the imaged area is limited exactly beneath the DAS cable. Using noncolinear channel pairs will expand the ray path

<sup>1.</sup> Seismological Laboratory, California Institute of Technology, Pasadena, California, U.S.A., https://orcid.org/0000-0001-6369-4802 (JF); https://orcid.org/0000-0002-6105-2918 (YY); https://orcid.org/0000-0002-3305-0982 (EB); https://orcid.org/0000-0002-6471-4497 (EFW); 2. Key Laboratory of Earth and Planetary Physics, Institute of Geology and Geophysics, Chinese Academy of Sciences, Beijing, China; 3. Department of Geological Sciences, California State University Long Beach, Long Beach, California, U.S.A., https://orcid.org/0000-0001-8242-0591 (MWB)

<sup>\*</sup>Corresponding author: jfang@caltech.edu

<sup>©</sup> Seismological Society of America

coverage of tomography but can complicate the interpretation of surface-wave observations and lower the signal-to-noise ratio (SNR) due to directional sensitivity. Although researchers have reported coherent signals from cross-correlations between different fiber-optic lines (Martin *et al.*, 2018), the interpretation of these signals remains unclear, and they are not commonly considered further in real data for surface-wave tomography.

Typically, city telecommunication cables have complex geometry. Directional sensitivity poses a challenge to signal interpretation when we want to employ these cable networks for seismic tomography. Attempts in different manners have been proposed to tackle this problem. For example, Paitz et al. (2019) discussed the possibility of an adjoint-based waveform inversion method using DAS data. Nevertheless, this method may be computationally expensive and involve more complications, including source distribution, cable coupling, and site effects (Sager et al., 2018). Luo et al. (2020) and Martin et al. (2021) undertook thorough theoretical investigations on fiberoptic strain interferometry and illustrated the directional sensitivity of various seismic waves. With appropriate cable configurations, it is possible that one kind of wave is dominant or different kinds of waves can be distinguished.

The approach of directional sensitivity analysis has not been tested with real DAS data so far. Here, we examine the directional sensitivity of DAS and the feasibility of 2D ambient noise tomography using a rectangular DAS array in the City of Oxnard, California. We compare dispersion curves at the same location illuminated by colinear and noncolinear virtual sources to interpret observed surface wave signals. Cross-correlation SNR is measured to evaluate the effects of directional sensitivity. We further present an example of DAS-based 2D ambient noise tomography in this area and demonstrate the potential of efficient subsurface imaging with multiple fiberoptic lines.

### **Data and Noise Interferometry**

Oxnard is a city located on the Santa Clara River delta in southern California, and we were granted access to a 14.7-kilometer-long cable network in the downtown area (Fig. 1). The Silixa iDAS v2 (Parker et al., 2014) turned these cables into 2496 virtual channels recording local strain rates, clockwise along the rectangle. The first 2370 channels have satisfactory records available for analysis. The channel spacing is 6.75 m, and the gauge length is set to 10 m. The instrument operated from 28 January to 13 March 2020 and collected an 8.3 TB continuous strain rate data at a sampling rate of 200 Hz.

For noise interferometry, we cross-correlate concurrent strain rate time series between different channel pairs following the standard workflow that was developed for conventional seismic data (Bensen *et al.*, 2007). The preprocessing procedure includes detrending, removing the mean, band-pass filtering to

0.1–10 Hz, and downsampling to 50 Hz. Data are then saved as hourly segments and transformed to frequency domain after a running-absolute-average temporal normalization. With spectral whitening applied, cross-correlation functions are calculated and normalized. In total, 1000 h of cross-correlations are transformed back to time domain and stacked for analysis.

The noise interferometry approach is established under assumptions of homogeneous noise source distribution or equipartitioned wavefield, but these idealized assumptions may not be strictly followed in practice. Particularly, previous studies have validated this tomographic method in coastal regions, where strong microseism from the ocean always causes heterogeneous noise source distribution (Castellanos and Clayton, 2021; Jia and Clayton, 2021). It is also justified by theoretical analyses that travel times, which ambient noise tomography focuses on, are generally insensitive to this kind of smooth, non-extreme noise source heterogeneity (Sager *et al.*, 2018).

# Analysis of Directional Sensitivity Directional sensitivity in theory

Unlike a conventional geophone that measures particle motion at a point, a DAS channel measures the average axial strain or strain rate over a gauge length of fiber. Here, we assume a simplified single-component geophone measuring particle velocity and a simplified DAS channel measuring strain rate, both in the  $(\cos\theta,\sin\theta,0)$  orientation. We let a plane wave described by particle velocity  $v(x,y,z,t)=(v_x(x,y,z,t),v_y(x,y,z,t),v_z(x,y,z,t))$ , in which x,y,z are spatial coordinates and t is time. When this wave reaches a geophone, the instrument would observe the velocity  $v_{\theta}(x,y,z,t)=v_x(x,y,z,t)\cos\theta+v_y(x,y,z,t)\sin\theta$ . For the same wave field, the pointwise axial strain rate in the same direction  $(\cos\theta,\sin\theta,0)$  is

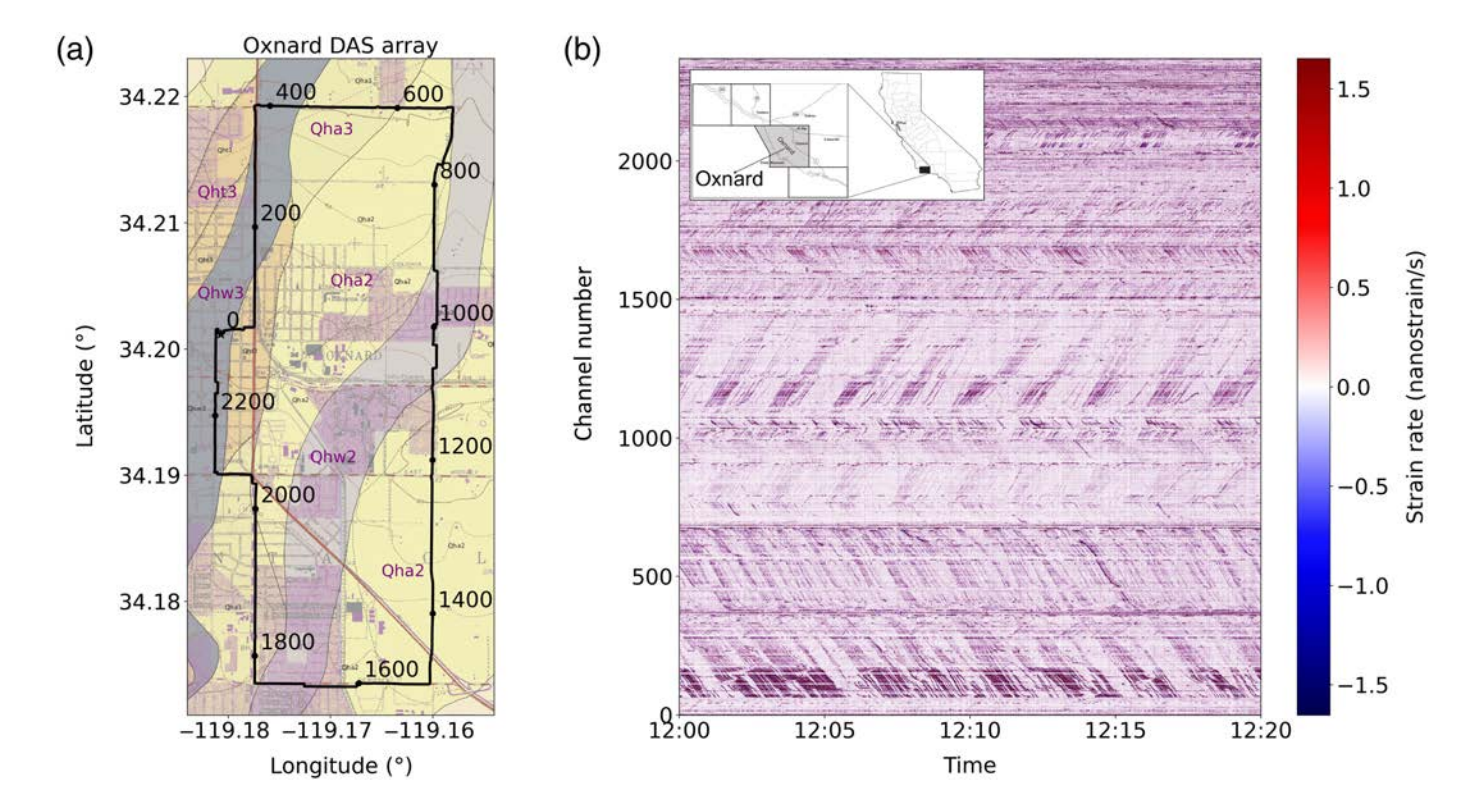
$$\dot{\epsilon}_{\theta}(x, y, z, t) = \frac{\partial v_x}{\partial x} \cos^2 \theta + \left(\frac{\partial v_x}{\partial y} + \frac{\partial v_y}{\partial x}\right) \cos \theta \sin \theta + \frac{\partial v_y}{\partial y} \sin^2 \theta.$$
(1)

A fiber-optic DAS channel in this direction will observe the average axial strain rate  $\dot{\epsilon}_{\theta,L}$  over a gauge length L:

$$\dot{\epsilon}_{\theta,L}(x,y,z,t) = \frac{1}{L} \int_{-\frac{L}{2}}^{\frac{L}{2}} \dot{\epsilon}_{\theta}(x,y,z,t) dl 
= \frac{1}{L} \int_{-\frac{L}{2}}^{\frac{L}{2}} \left[ \frac{\partial v_x}{\partial x} \cos^2 \theta + \left( \frac{\partial v_x}{\partial y} + \frac{\partial v_y}{\partial x} \right) \cos \theta \sin \theta + \frac{\partial v_y}{\partial y} \sin^2 \theta \right] dl. \quad (2)$$

When the wavelength of the plane wave is substantially larger than the gauge length, the previous equation can be simplified as follows:

$$\dot{\epsilon}_{\theta,L}(x,y,z,t) \approx \dot{\epsilon}_{\theta}(x,y,z,t) = \frac{\partial \nu_x}{\partial x} \cos^2 \theta + \left(\frac{\partial \nu_x}{\partial y} + \frac{\partial \nu_y}{\partial x}\right) \cos \theta \sin \theta + \frac{\partial \nu_y}{\partial y} \sin^2 \theta.$$
 (3)



When DAS measures the axial component of the strain tensor, Martin *et al.* (2021) has calculated theoretical sensitivity of plane Rayleigh and Love-wave cross-correlation functions in a homogeneous half-space. We assume two DAS channels in the  $(\cos\theta_1,\sin\theta_1,0)$  and  $(\cos\theta_2,\sin\theta_2,0)$  orientations, measuring strain rate time series  $\dot{\epsilon}_{\theta_1}(t)$  and  $\dot{\epsilon}_{\theta_2}(t)$ , respectively, and the direction of the line between these two channels is denoted by  $\phi$  (Fig. 2). The cross-correlation of two concurrent time series is given as  $\dot{\epsilon}_{\theta_1}*\dot{\epsilon}_{\theta_2}=\frac{1}{2T}\int_{-T}^T\dot{\epsilon}_{\theta_1}(t)\dot{\epsilon}_{\theta_2}(t+\tau)\mathrm{d}t$ , in which  $\tau$  is the time lag and T is the maximum time of data. For Rayleigh waves, the signal amplitude in the cross-correlation (Fig. 2a) is described by

$$|\dot{\epsilon}_{\theta_1} * \dot{\epsilon}_{\theta_2}| \propto \cos^2(\theta_1 - \phi) \cos^2(\theta_2 - \phi).$$
 (4)

For Love waves, the signal amplitude of the cross-correlation (Fig. 2b) is described by

$$|\dot{\epsilon}_{\theta_1} * \dot{\epsilon}_{\theta_2}| \propto \frac{1}{4} |\sin 2(\theta_1 - \phi) \sin 2(\theta_2 - \phi)|.$$
 (5)

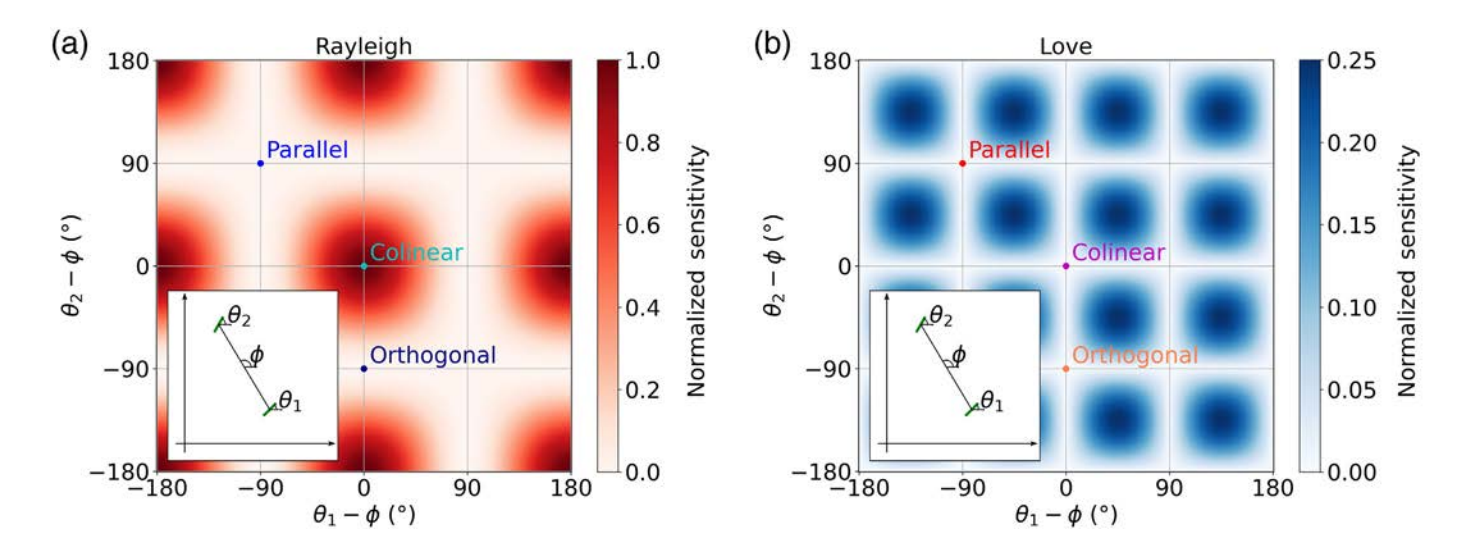
If a pair of channels are in radial–radial alignment  $(\theta_1 = \theta_2 = \phi)$ , DAS cross-correlation functions have the maximum sensitivity to Rayleigh waves and zero sensitivity to Love waves. That validates previous studies that employ colinear DAS channels for Rayleigh-wave tomography. When  $\theta_1 - \phi \neq 0$  or  $\theta_2 - \phi \neq 0$ , the sensitivity of DAS cross-correlation functions to Rayleigh waves decays rapidly, and the sensitivity to Love waves gradually increases. Consequently, both Rayeleigh and Love wave signals can coexist in noise

Figure 1. The location of the Oxnard distributed acoustic sensing (DAS) array and seismic data obtained from this array. (a) The configuration map of the Oxnard DAS array. The DAS array is shown in black, with channel numbers annotated. It starts from channel 0 and goes clockwise, via Second Street (west-east), Oxnard Boulevard (south-north), Gonzales Road (west-east), Rose Avenue (north-south), Channel Island Boulevard (eastwest), Saviers Road (south-north), Wooley Road (east-west), and C Street (south-north), forming a closed loop. The background is the near-surface geologic map of this area (Clahan, 2003). The DAS array crosses units Qhw3 (newer Holocene wash deposits), Qht3 (newer Holocene stream terrace deposits associated with Qhw3), Qha3 (newer Holocene alluvial deposits associated with Qhw3), Qhw2 (older Holocene wash deposits), and Qha2 (older Holocene alluvial deposits associated with Qhw2). (b) An example 20 min records from the Oxnard DAS array. The inset shows the location of Oxnard in California. The color version of this figure is available only in the electronic edition.

interferometry results at a relatively low SNR and may not be separable, increasing the difficulty to identify one wave type for use in tomography.

#### Directional sensitivity in the data

The cross-correlations of a virtual source with other channels reveal propagating surface wave signals that can be clearly traced (Fig. 3). The signals for channels located along the same line have the highest SNR and can be confidently identified as Rayleigh-wave fundamental mode based on the aforementioned theoretical analysis. For some other channels on parallel



**Figure 2.** Theoretical directional sensitivity of two kinds of surface waves for different channel pair configurations.  $\theta_1$  and  $\theta_2$  denote orientations of two channels, and  $\phi$  denotes the direction of the

line between these two channels. (a) Rayleigh wave, calculated from equation (4). (b) Love wave calculated from equation (5). The color version of this figure is available only in the electronic edition.

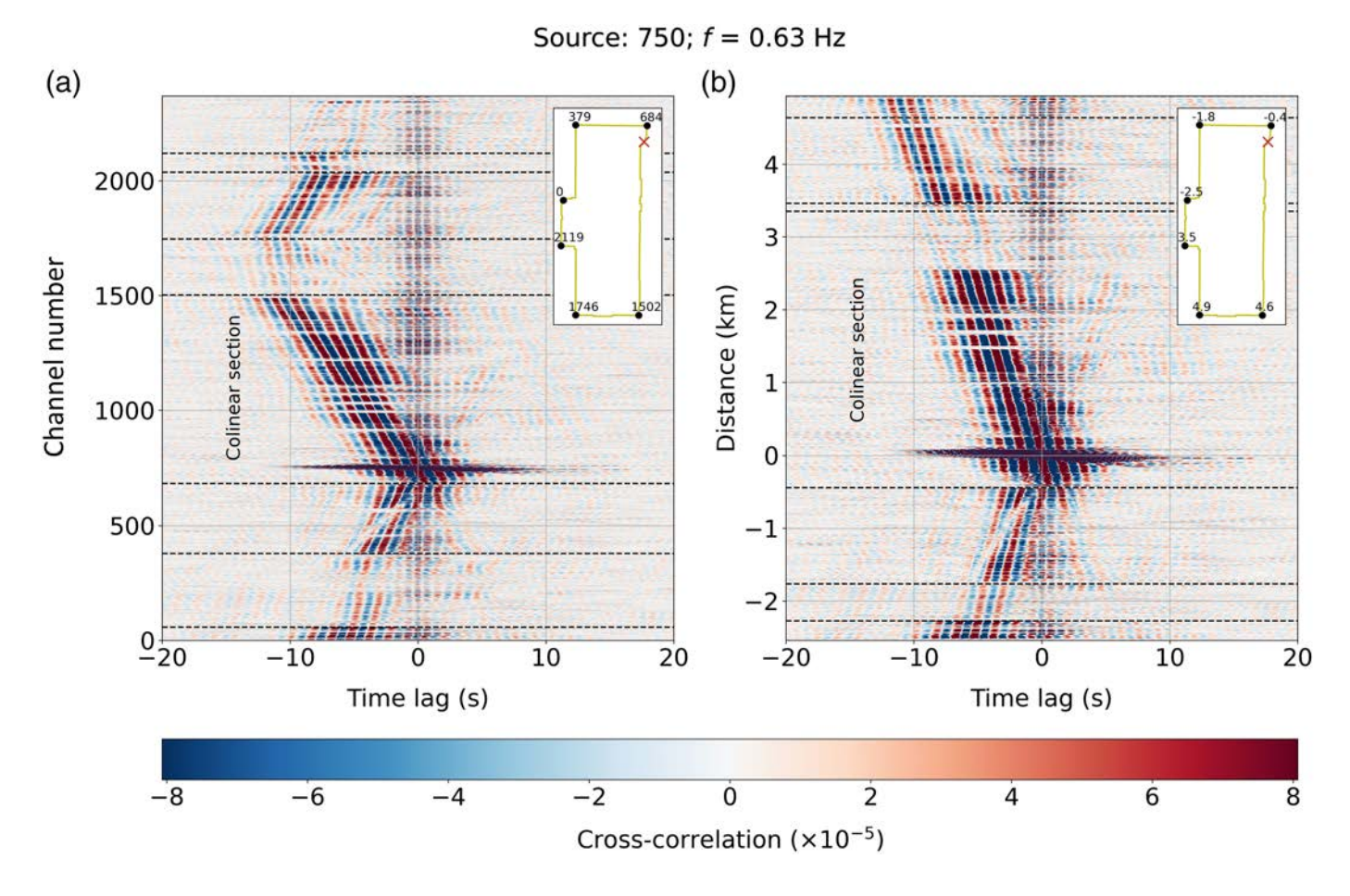
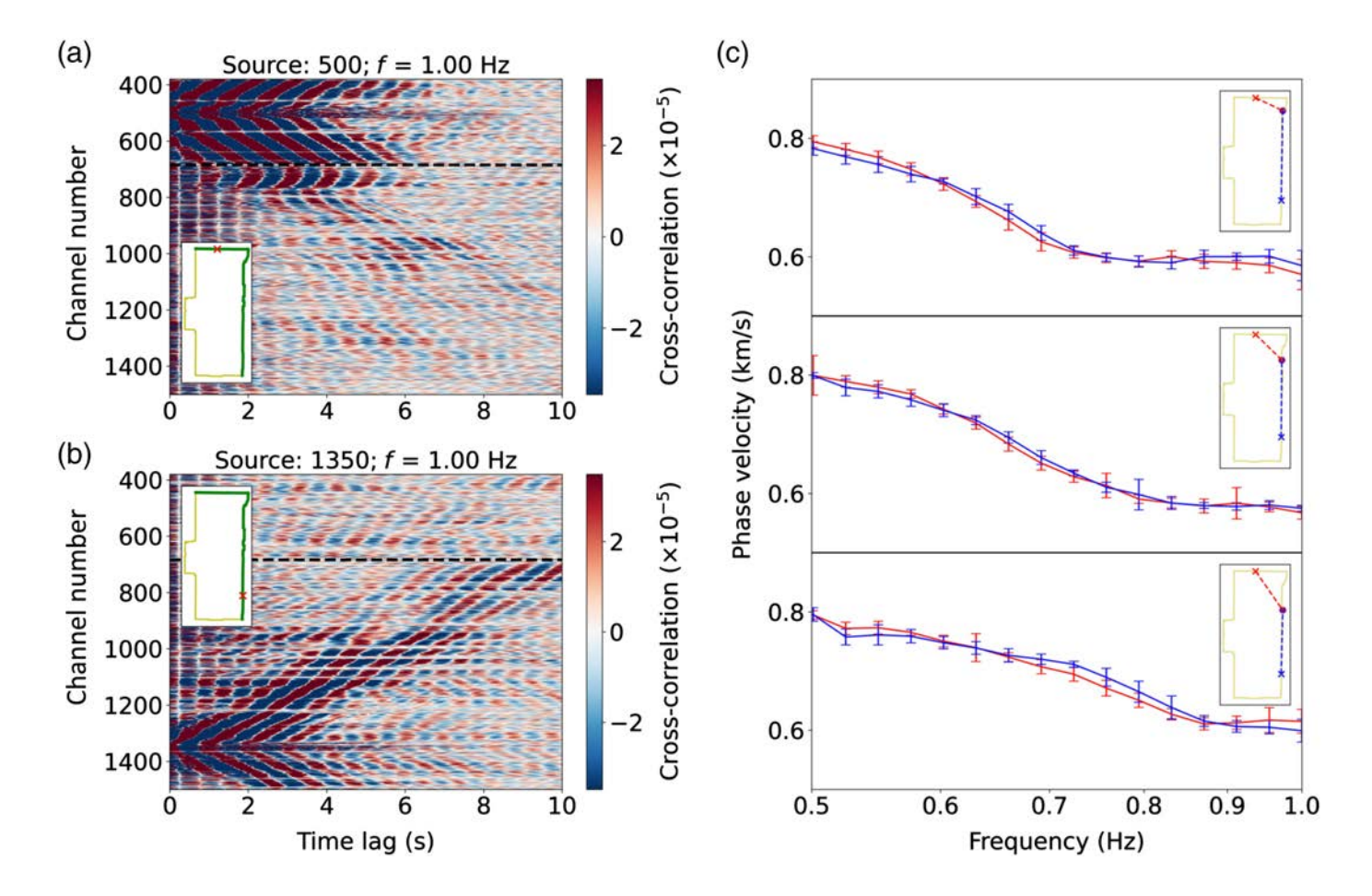


**Figure 3.** An example shot gather of cross-correlation functions along the Oxnard DAS array at 0.63 Hz, with the virtual source at channel 750 on the north–south section along the Rose Avenue. (a) Cross-correlation functions for all channels along the DAS array. The inset shows the virtual source (red cross) and channel numbers corresponding to turning points (annotated black dots). (b) Cross-correlation functions for channels at different distances

to the virtual source. Channels with channel numbers smaller than the virtual source have negative distance values, and channels with channel numbers larger than the virtual source have positive distance values. The inset shows the virtual source (red cross) and distances corresponding to turning points (annotated black dots). The color version of this figure is available only in the electronic edition.

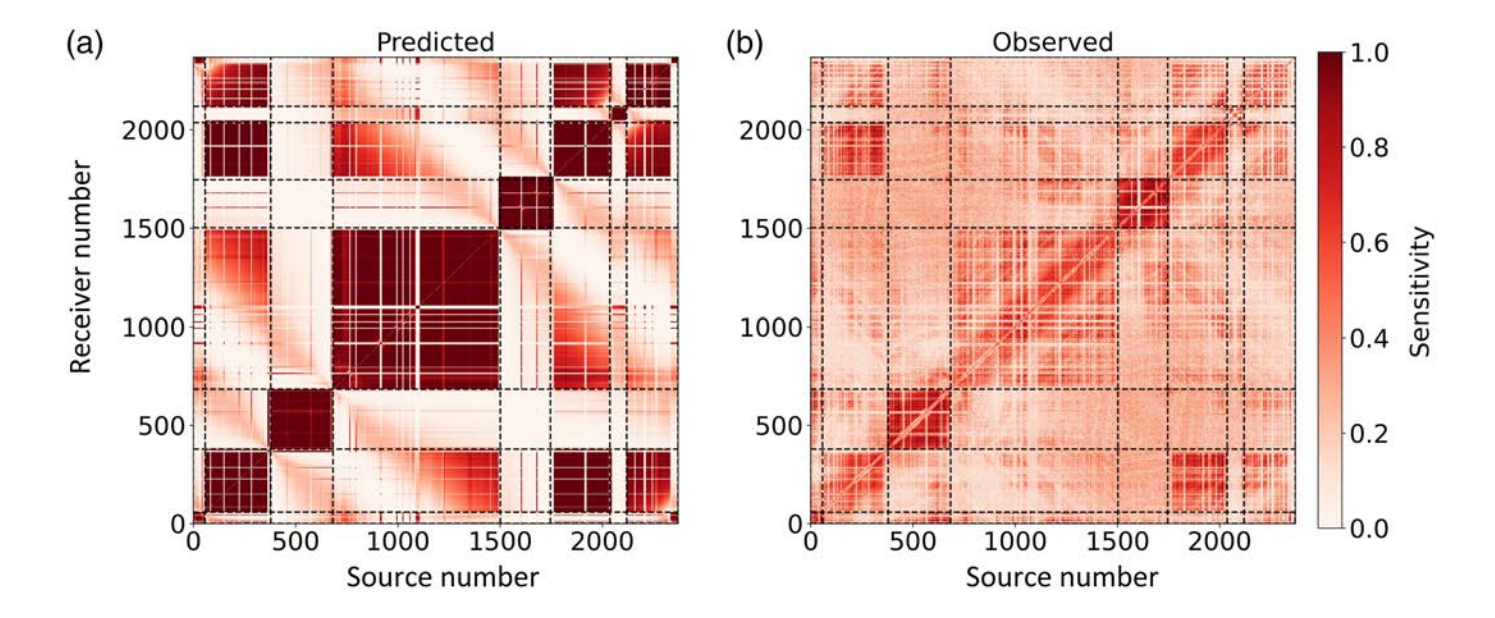


or orthogonal lines, the signals are still prominent and appear congruous with radial-radial channel pairs. A quantitative analysis of the consistency is performed by comparing the phase velocity dispersion of channel pairs in different configurations. To extract dispersion curves from the cross-correlations, we select a subarray around the measuring channel and utilize a beamforming method, shifting the waveforms based on a wide range of phase velocities for each narrow frequency band in 0.5-1 Hz and searching for the optimal value that can maximize the stacked energy (Näsholm et al., 2022; Yang, Atterholt, et al., 2022). The anticausal and causal parts are averaged to address possible signal amplitude asymmetry, and the subarray size is twice the estimated wavelength assuming a reference phase velocity at each frequency. Repeated measurements are made by treating other channels on the same line as the virtual source, and final results are produced from the mean with the uncertainties taken from the standard deviation. As shown in Figure 4, regardless of how the virtual source is oriented, the phase velocity measurements do not show significant variations. The two average dispersion curves measured at the same location, illuminated by colinear and noncolinear virtual sources, respectively, are consistent within measurement uncertainty. Because dispersion curves extracted from the colinear cross-correlations are supposed to be associated with Rayleigh waves, the signals in noncolinear cross correlations are likely to be dominated by longitudinally

**Figure 4.** DAS noise interferometry results along the west–east section along Gonzales Avenue and the north–south section along Rose Avenue. (a) A shot gather at 1 Hz, with the virtual source (red cross) on the west–east section. The green segment in the inset displays the range of receivers in the record section. The black dashed line denotes the bend between two fiber-optic lines. (b) A shot gather at 1 Hz, with the virtual source on the north–south section. (c) Comparison of phase velocity dispersion curves of the same locations (purple dot) on the north–south section illuminated by a colinear virtual source (blue cross) and an orthogonal virtual source (red cross). The color version of this figure is available only in the electronic edition.

polarized Rayleigh waves in light of the dispersion curve consistency.

We calculate the SNR for cross-correlation functions of all channel pairs along this rectangular DAS array. When SNRs on the anticausal and causal sides differ, the higher one is considered. For each channel pair, the SNR value is compensated for attenuation by multiplying the ratio of the maximum SNR of colinear channel pairs with the same distance to the reference SNR of an adjacent colinear channel pair for which attenuation can be ignored. As shown in Figure 5, although there are more complexities possibly caused by cable coupling, the observed SNR map at a certain frequency is generally consistent with the theoretically predicted sensitivity. It is confirmed that



channel pairs with different orientations vary in cross-correlation SNRs over all frequency bands, with colinear channel pairs exhibiting a higher SNR. In particular, some pairs (e.g., with sources in 0-400 and receiver in 700-1500) show a change in SNR with angles that compare favorably with the theoretical analysis. This comparison suggests that the influence of directional sensitivity is evident in DAS ambient noise interferometry and should be carefully evaluated in future studies. In this dataset, despite the expected reduced amplitude for noncolinear cross-correlation functions, there are still Rayleigh-wave observations that can be tracked. These prevalent Rayleigh wave signals enable 2D tomography of areas inside the rectangle between cables.

## **DAS-Based 2D Rayleigh-Wave Tomography** Method

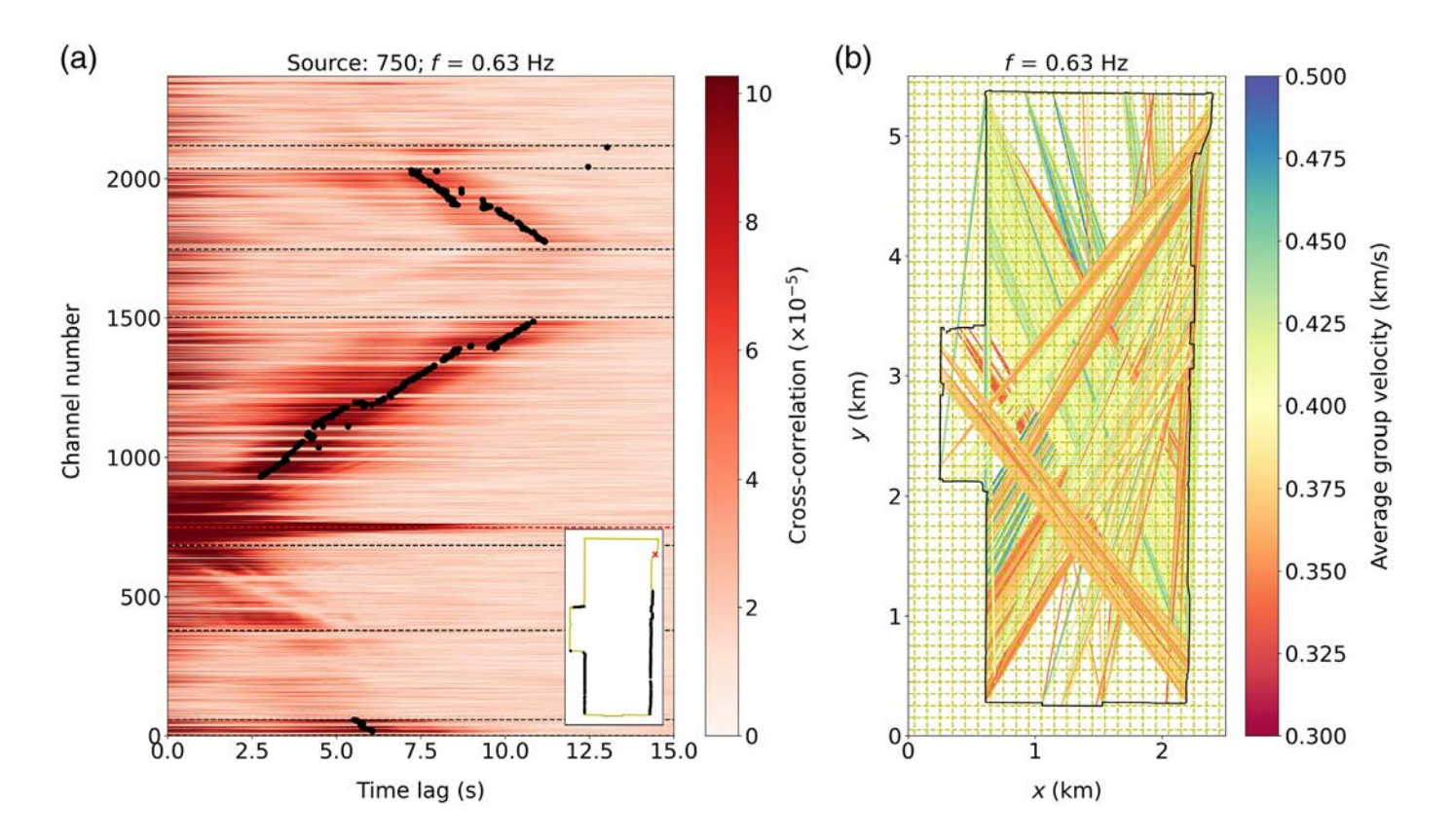
Because Rayleigh wave signals are dominant in most crosscorrelation functions in the frequency band of 0.5-1 Hz, we can invert for the retrieved Rayleigh-wave dispersion maps independently at various frequencies, which can ultimately be combined to construct shear-wave velocity models at different depths. Here, we switch from local phase velocity beneath a channel to the average group velocity over the ray path between a pair of channels because these group velocity measurements sample areas between fiber lines and are computationally efficient to obtain. We demonstrate this method at a frequency of 0.63 Hz, in which data quality is the best for this DAS array. For higher frequencies, attenuation and contamination by higher-mode overtones greatly influence the extraction of Rayleigh-wave group travel time. If the frequency is lower, the wavelength will become comparable with the scale of the DAS array, and the interference of signals in anticausal and causal parts will make travel-time measurements inaccurate. The cross-correlation of each channel pair

Figure 5. Comparison of predicted and observed sensitivity of Rayleigh wave signals in the noise interferometry results. (a) The sensitivity calculated from equation (4). (b) The sensitivity inferred from signal-to-noise ratios (SNRs) in cross-correlation functions between different channel pairs. Because the cross-correlation factors are normalized and the noise energy is similar within this area, SNRs can well represent the sensitivity. The values are compensated for attenuation. The color version of this figure is available only in the electronic edition.

corresponds to a ray path for which we can extract the propagating Rayleigh wave signal. At this given frequency, group travel times of ray paths are first measured by applying a narrow band-pass filter, performing the Hilbert transform to extract envelope, averaging the anticausal and causal sides, and then taking the time lag corresponding to the maximum amplitude.

As previously shown, noncolinear configurations are projected to have weaker sensitivity of Rayleigh-wave cross-correlations. Some of these channel pairs produce low-SNR observations and yield erroneous travel times, so a careful quality control is essential. Channel pairs with a short separation compared with the wavelength are first excluded. Maximum and minimum group velocities are imposed, and measurements outside the interval are disregarded. Assuming the near-surface velocity is relatively smooth and invariable, we perform RANdom SAmple Consensus linear regression (Fischler and Bolles, 1981; Pedregosa et al., 2011) for a fixed virtual source and channels aligned on the same line, and outliers farther away from the best-fit distance-time line are also rejected. The selected travel measurements that are employed for group velocity inversion are shown in Figure 6.

The standard grid-based inversion scheme is applied to derive a 2D group velocity map inside the rectangular array.



A square block parameterization is employed for the inversion, with a discretization  $\Delta x = 100$  m in each direction, and straight ray paths are assumed. Each ray path is divided into 200 evenly spaced segments, and the square center that is closest to the center of a segment defines a square containing that segment. We use a uniform initial model taken from the average group slowness from all ray paths. A damped least squares inversion is performed, with damping parameters selected from the L curve to balance the model misfit and roughness (Tarantola, 2005; Aster *et al.*, 2018).

#### Results

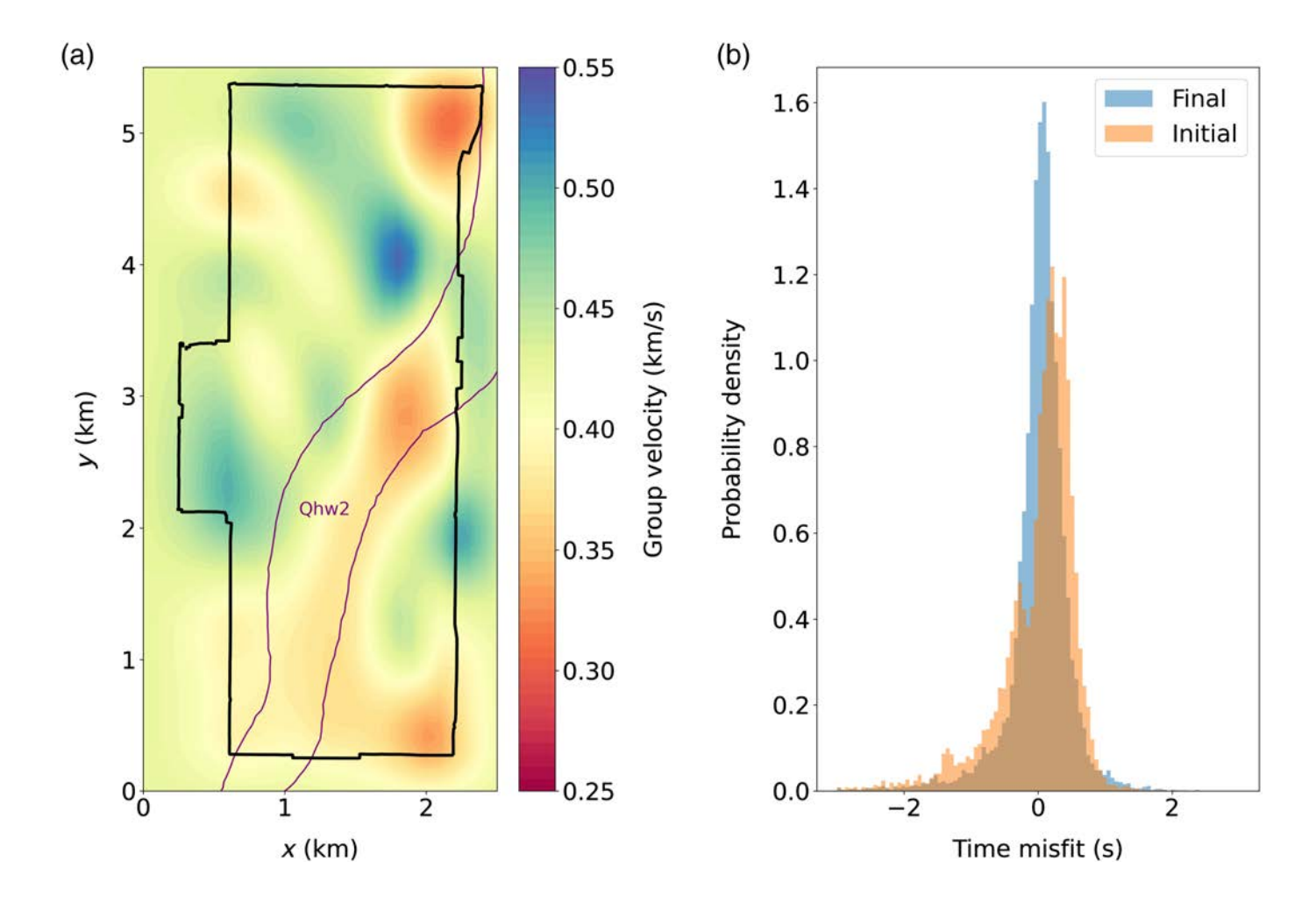
We successfully obtain a Rayleigh-wave group velocity map at a frequency of 0.63 Hz (Fig. 7a) with this inversion framework, and the workflow can be extended to other frequencies close to 0.63 Hz (Fig. S1, available in the supplemental material to this article). The residuals are statistically reduced, which verifies the success of the inversion (Fig. 7b). Notably, there is a prominent low-velocity anomaly in the southern part of the study area, for which location coincides with an ancient river channel in the geologic map (Clahan, 2003). The group velocity in this study is sensitive to shear-wave velocity structures in the top 400 m based on the sensitivity kernel (Fig. S2) computed from the Southern California Earthquake Center velocity model, CVM-S4.26.M01 (Herrmann, 2013; Lee et al., 2014). In the top layers, wash sediments within the river should be softer than alluvial sediments deposited nearby, which is consistent with the observed low-velocity anomaly.

**Figure 6.** (a) An example pick of Rayleigh-wave group travel times. The background is a shot gather after Hilbert transform at 0.63 Hz, with the virtual source at channel 750. The black dots denote picked Rayleigh-wave travel times for different channels after quality control. The inset shows the virtual source (red cross) and channels with picked travel times (black dots). (b) Rayleigh wave ray paths used in the grid-based inversion, colored in their average velocities. The color version of this figure is available only in the electronic edition.

#### Discussion

We observe apparent surface wave signals in DAS cross-correlation functions across a broad range of channel orientations and demonstrate that they are mainly Rayleigh wave signals through comparison of dispersion curves. The observed dominance of Rayleigh waves is central to overcoming the interpretation ambiguity in noncolinear cross correlations, which is the principal barrier to DAS-based 2D ambient noise imaging. However, the Rayleigh-wave SNR of noncolinear cross-correlation pairs is systematically lower than that of colinear pairs, which requires us to implement multilevel quality control procedures to reject problematic measurements before performing a tomographic inversion.

Oxnard is close to the Pacific coast. This special environment with abundant ocean-generated microseism noise can explain the dominance of Rayleigh waves in most cross-correlation functions calculated from this dataset. Ocean waves can be the predominant noise source at the frequency band we are studying (0.5–1 Hz), and wave–wave or wave–bathymetry



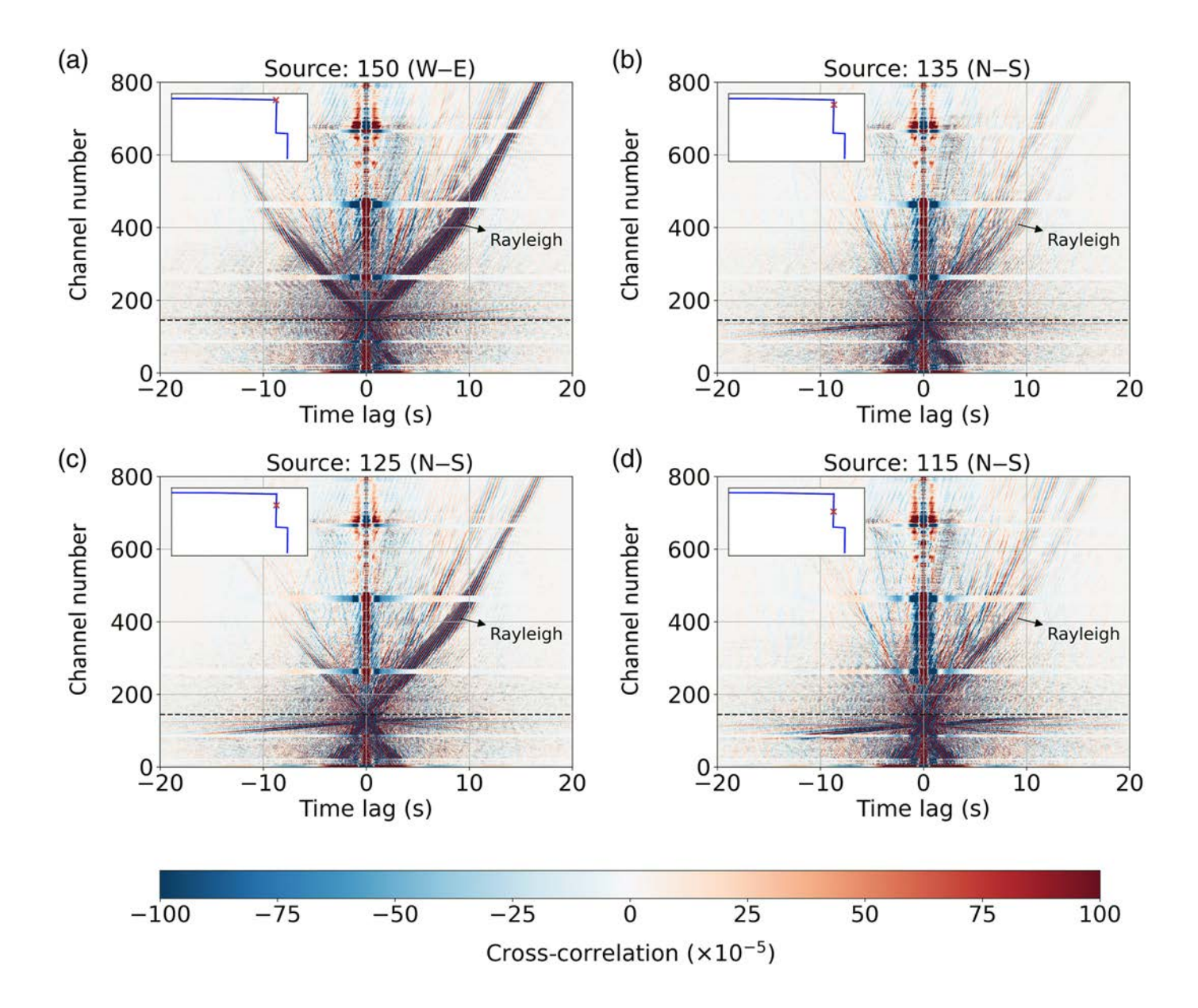
interactions generate strong noise that mainly contain Rayleigh waves (Hasselmann, 1963; Tanimoto, 2007; Koper et al., 2010). The directional asymmetry between positive and negative time lags in cross-correlations (e.g., Fig. 3) indicates that the observed Rayleigh waves are predominately traveling across the array from southwest to northeast, which supports the interpretation of a local oceanic source. Because ambient noise Love waves originate from propagation effects rather than directly as a result of wave-wave interaction in the ocean (Le Pape et al., 2021), the proximity of Oxnard to the coast may partly explain the lack of Love wave signals. This is consistent with previous observations of high ambient noise Rayleigh-to-Love wave ratios in southern California (Tanimoto et al., 2016; Gualtieri et al., 2020).

In some configurations in which theory predicts minimal sensitivity (e.g., nearly orthogonal channel pairs), the crosscorrelation data still display Rayleigh wave signals. Small-scale complexity in the cable configuration (e.g., loops and bends) can contribute to these amplified observations. Local heterogeneity adjacent to cables may also affect DAS strain measurements (Muir and Zhan, 2022). Moreover, a small amount of Rayleigh waves can be deviated from straight trajectories as a result of scattering, which magnifies signals for nonoptimal channel pair orientations (Yang, Zhan, et al., 2022).

Figure 7. The inversion results. (a) The Rayleigh-wave group velocity map at 0.63 Hz. The purple lines in the inset figure represent the boundary of Qhw2 zone with an ancient river channel. (b) Histogram of travel-time residuals before and after the inversion. The color version of this figure is available only in the electronic edition.

Particularly, thick, poorly consolidated river delta sediments underlying the city, as well as urban infrastructure such as multilevel basements and underground parking structures, can intrinsically lead to significant wave scattering (Johnson and Silva, 1981; Malagnini et al., 1995; Pitilakis and Tsinidis, 2014). Although it is plausible that these effects have a secondary impact, signal amplitudes in cross-correlations are still primarily controlled by the theoretical directional sensitivity of DAS.

The opportunity for 2D ambient noise tomography using one type of identified surface wave should not be limited to Oxnard. In other coastal regions, locally generated ocean microseism is also expected to be the main noise source and resulting Rayleigh waves prevail over Love waves. Recently, emerging submarine DAS experiments are providing insight into subsurface structures beneath offshore areas (Lindsey et al., 2019; Williams et al., 2019), and the efficiency of tomography is a major concern.



Previous research has discovered the dominance of Scholte waves, the underwater counterpart of Rayleigh waves, in interferometry results of submarine DAS data (Williams *et al.*, 2021) because ocean-related microseism serves as the primary noise source. Integration of data from cables in a proper noncolinear configuration enables 2D ambient noise tomography of the seafloor, which is more cost-effective than traditional approaches.

Similar imaging work may also be feasible for inland DAS arrays where seismic ambient noise is predominately generated by vehicle traffic. From another DAS array deployed in the City of Ridgecrest, California, we have more than one year of continuous seismic records, and we can obtain extremely high-SNR noise interferometry results with data over that long period (Li et al., 2021; Yang, Atterholt, et al., 2022). Several propagating signals can be retrieved in noncolinear cross-correlation functions (Fig. 8). After comparing them with signals in colinear cross-correlations, we can identify consistent Rayleigh waves that can be incorporated into future tomography. This example

**Figure 8.** Example shot gathers from the Ridgecrest DAS array. Rayleigh wave signals are annotated and can be clearly traced in the causal part for every virtual source regardless of its location and orientation. The insets show the location of each virtual source (red cross) on the DAS array (blue line). (a) The virtual source is in the west—east direction. The strongest signal is expected to be the direct arrival of Rayleigh-wave fundamental mode. (b,c,d) The virtual sources are in the north—south direction. Signals consistent with the Rayleigh-wave fundamental mode can be observed. The color version of this figure is available only in the electronic edition.

indicates the broad applicability of our method in a variety of environments. Notably, other waves, possibly Rayleigh-wave higher-mode overtones, Love waves, or body waves, also occur, and they can supply more information about the subsurface if appropriately interpreted. The interpretation of multiple wave signals and potential joint tomography can be another focus of future studies.

#### **Conclusions**

We report an experimental analysis of DAS directional sensitivity and DAS-based 2D ambient noise tomography in Oxnard, California. Although Rayleigh-wave SNR decreases for noncolinear cross-correlation pairs in accordance with theory, we can still track surface wave signals in noncolinear cross-correlations and identify them as Rayleigh waves by comparing dispersion curves. The dominance of Rayleigh waves in observations, linked to predominant ocean-generated microseism noise near the Pacific coast, is a prerequisite for imaging 3D structures inside the rectangular DAS array. With a multilevel quality control algorithm to select reliable measurements and a conventional grid-based inversion, we can efficiently construct a high-resolution Rayleigh-wave dispersion map, which can ultimately be inverted to a true 3D shear-velocity model. The tomography results successfully recover fine-scale geological structures. We suggest that this workflow also applies to other areas where one type of surface waves dominates or can be separated. This study demonstrates that DAS is capable of high-resolution subsurface imaging in 3D and can be effective in subsurface structure identification and urban seismic hazard analysis.

#### **Data and Resources**

The noise cross-correlations for producing all the results can be downloaded from CaltechDATA at doi: 10.22002/D1.20221 in the Program for Array Seismic Studies of the Continental Lithosphere (PASSCAL) SEG-Y format, with the script to read PASSCAL SEG-Y files enclosed. This file contains cross-correlation functions for all 2370 × 2370 channel pairs, with time lags between -30 and 30 s. The geologic map of Oxnard can be found at https://filerequest.conservation.ca.gov/?q=oxnard\_prelim.pdf (last accessed October 2022). The supplemental material includes two figures to support the main text. Figure S1 presents Rayleigh-wave group velocity maps at 0.60, 0.63, and 0.66 Hz, as a supplement of the result at 0.63 Hz (Fig. 7a). Figure S2 shows the sensitivity kernels of Rayleigh-wave group velocity at these frequencies computed from the reference CVM-S4.26.M01 model.

# **Declaration of Competing Interests**

The authors acknowledge that there are no conflicts of interest recorded.

#### **Acknowledgments**

The authors are grateful to the City of Oxnard, California, for access to their fiber-optic network and the support provided by Mike Shaffer, the City of Oxnard's GIS manager. The iDAS v2 system is supported by National Science Foundation (NSF) Grant Number MRI-1920334. Z. Z. acknowledges support from the Moore Foundation, NSF Faculty Early Career Development Program (CAREER) Award Number 1848166, and U.S. Geological Survey (USGS) Grant Number G22AP00067. J. F. and Z. Z. thank Weiqiang Zhu, Wenbo Wu, and Yida Li for helpful discussions. The authors also appreciate constructive comments and suggestions from two anonymous reviewers.

#### References

- Ajo-Franklin, J. B., S. Dou, N. J. Lindsey, I. Monga, C. Tracy, M. Robertson, V. Rodriguez Tribaldos, C. Ulrich, B. Freifeld, et al. (2019). Distributed acoustic sensing using dark fiber for near-surface characterization and broadband seismic event detection, Sci. Rep. 9, no. 1, 1–14.
- Aki, K. (1993). Local site effects on weak and strong ground motion, *Tectonophysics* **218**, nos. 1/3, 93–111.
- Aster, R. C., B. Borchers, and C. H. Thurber (2018). *Parameter Estimation and Inverse Problems*, Elsevier, Amsterdam, Netherlands.
- Bensen, G., M. Ritzwoller, M. Barmin, A. L. Levshin, F. Lin, M. Moschetti, N. Shapiro, and Y. Yang (2007). Processing seismic ambient noise data to obtain reliable broad-band surface wave dispersion measurements, *Geophys. J. Int.* 169, no. 3, 1239–1260.
- Bianco, M. J., P. Gerstoft, K. B. Olsen, and F.-C. Lin (2019). High-resolution seismic tomography of Long Beach, CA using machine learning, *Sci. Rep.* **9**, no. 1, 1–11.
- Borcherdt, R. D., and J. F. Gibbs (1976). Effects of local geological conditions in the San Francisco Bay region on ground motions and the intensities of the 1906 earthquake, *Bull. Seismol. Soc. Am.* **66**, no. 2, 467–500.
- Castellanos, J. C., and R. W. Clayton (2021). The fine-scale structure of Long Beach, California, and its impact on ground motion acceleration, *J. Geophys. Res.* **126**, no. 12, e2021JB022462, doi: 10.1029/2021JB022462.
- Clahan, K. (2003). Geologic map of the Oxnard 7.5' Quadrangle Ventura County, California: A digital database, U.S. Geol. Surv. California Geol. Surv.
- Dou, S., N. Lindsey, A. M. Wagner, T. M. Daley, B. Freifeld, M. Robertson, J. Peterson, C. Ulrich, E. R. Martin, and J. B. Ajo-Franklin (2017). Distributed acoustic sensing for seismic monitoring of the near surface: A traffic-noise interferometry case study, *Sci. Rep.* 7, no. 1, 1–12.
- Fischler, M. A., and R. C. Bolles (1981). Random sample consensus: A paradigm for model fitting with applications to image analysis and automated cartography, *Commun. ACM* **24**, no. 6, 381–395.
- Graves, R. W., A. Pitarka, and P. G. Somerville (1998). Ground-motion amplification in the Santa Monica area: Effects of shallow basin-edge structure, *Bull. Seismol. Soc. Am.* 88, no. 5, 1224–1242.
- Gualtieri, L., E. Bachmann, F. J. Simons, and J. Tromp (2020). The origin of secondary microseism Love waves, *Proc. Natl. Acad. Sci. Unit. States Am.* **117**, no. 47, 29,504–29,511.
- Hasselmann, K. (1963). A statistical analysis of the generation of microseisms, *Rev. Geophys.* **1,** no. 2, 177–210.
- Herrmann, R. B. (2013). Computer programs in seismology: An evolving tool for instruction and research, *Seismol. Res. Lett.* **84**, no. 6, 1081–1088.
- Jia, Z., and R. W. Clayton (2021). Determination of near surface shearwave velocities in the central Los Angeles basin with dense arrays, *J. Geophys. Res.* **126**, no. 5, e2020JB021369.
- Johnson, L. R., and W. Silva (1981). The effects of unconsolidated sediments upon the ground motion during local earthquakes, *Bull. Seismol. Soc. Am.* 71, no. 1, 127–142.
- Koper, K. D., K. Seats, and H. Benz (2010). On the composition of earth's short-period seismic noise field, *Bull. Seismol. Soc. Am.* **100,** no. 2, 606–617.

- Kuvshinov, B. (2016). Interaction of helically wound fibre-optic cables with plane seismic waves, *Geophys. Prospect.* **64**, no. 3, 671–688.
- Le Pape, F., D. Craig, and C. J. Bean (2021). How deep ocean-land coupling controls the generation of secondary microseism Love waves, *Nat. Commun.* 12, no. 1, 1–15.
- Lee, E.-J., P. Chen, T. H. Jordan, P. B. Maechling, M. A. Denolle, and G. C. Beroza (2014). Full-3-D tomography for crustal structure in southern California based on the scattering-integral and the adjoint-wavefield methods, J. Geophys. Res. 119, no. 8, 6421–6451.
- Li, Z., Z. Shen, Y. Yang, E. Williams, X. Wang, and Z. Zhan (2021). Rapid response to the 2019 Ridgecrest earthquake with distributed acoustic sensing, *AGU Adv.* **2**, no. 2, e2021AV000395.
- Lim Chen Ning, I., and P. Sava (2018). Multicomponent distributed acoustic sensing: Concept and theory, *Geophysics* 83, no. 2, P1–P8.
- Lin, F.-C., D. Li, R. W. Clayton, and D. Hollis (2013). High-resolution 3D shallow crustal structure in Long Beach, California: Application of ambient noise tomography on a dense seismic array, *Geophysics* 78, no. 4, O45–O56.
- Lindsey, N. J., and E. R. Martin (2021). Fiber-optic seismology, *Annu. Rev. Earth Planet. Sci.* **49**, 309–336.
- Lindsey, N. J., T. C. Dawe, and J. B. Ajo-Franklin (2019). Illuminating seafloor faults and ocean dynamics with dark fiber distributed acoustic sensing, *Science* 366, no. 6469, 1103–1107.
- Lindsey, N. J., H. Rademacher, and J. B. Ajo-Franklin (2020). On the broadband instrument response of fiber-optic DAS arrays, J. Geophys. Res. 125, no. 2, e2019JB018145, doi: 10.1029/2019JB018145.
- Luo, B., W. Trainor-Guitton, E. Bozdağ, L. LaFlame, S. Cole, and M. Karrenbach (2020). Horizontally orthogonal distributed acoustic sensing array for earthquake-and ambient-noise-based multichannel analysis of surface waves, *Geophys. J. Int.* 222, no. 3, 2147–2161.
- Malagnini, L., R. B. Herrmann, G. Biella, and R. de Franco (1995). Rayleigh waves in Quaternary alluvium from explosive sources: Determination of shear-wave velocity and Q structure, *Bull. Seismol. Soc. Am.* **85**, no. 3, 900–922.
- Martin, E. R., F. Huot, Y. Ma, R. Cieplicki, S. Cole, M. Karrenbach, and B. L. Biondi (2018). A seismic shift in scalable acquisition demands new processing: Fiber-optic seismic signal retrieval in urban areas with unsupervised learning for coherent noise removal, *IEEE Signal Process. Mag.* **35**, no. 2, 31–40.
- Martin, E. R., N. J. Lindsey, J. B. Ajo-Franklin, and B. L. Biondi (2021). Introduction to interferometry of fiber-optic strain measurements, in *Distributed Acoustic Sensing in Geophysics: Methods and Applications*, 111–129.
- Michael, A. J., and D. Eberhart-Phillips (1991). Relations among fault behavior, subsurface geology, and three-dimensional velocity models, *Science* **253**, no. 5020, 651–654.
- Muir, J. B., and Z. Zhan (2022). Wavefield-based evaluation of DAS instrument response and array design, *Geophys. J. Int.* **229**, no. 1, 21–34.
- Näsholm, S. P., K. Iranpour, A. Wuestefeld, B. D. Dando, A. F. Baird, and V. Oye (2022). Array signal processing on distributed acoustic sensing data: Directivity effects in slowness space, *J. Geophys. Res.* **127,** no. 2, e2021JB023587.
- Nishida, K., J.-P. Montagner, and H. Kawakatsu (2009). Global surface wave tomography using seismic hum, *Science* **326**, no. 5949, 112–112.

- Olsen, K., S. Day, J. Minster, Y. Cui, A. Chourasia, M. Faerman, R. Moore, P. Maechling, and T. Jordan (2006). Strong shaking in Los Angeles expected from southern San Andreas earthquake, *Geophys. Res. Lett.* **33**, no. 7, doi: 10.1029/2005GL025472.
- Paitz, P., K. Sager, and A. Fichtner (2019). Rotation and strain ambient noise interferometry, *Geophys. J. Int.* 216, no. 3, 1938–1952.
- Parker, T., S. Shatalin, and M. Farhadiroushan (2014). Distributed acoustic sensing—A new tool for seismic applications, *First Break* **32**, no. 2, doi: 10.3997/1365-2397.2013034.
- Pedregosa, F., G. Varoquaux, A. Gramfort, V. Michel, B. Thirion, O. Grisel, M. Blondel, P. Prettenhofer, R. Weiss, V. Dubourg, et al. (2011). Scikit-learn: Machine learning in python, J. Machine Learn. Res. 12, 2825–2830.
- Pitilakis, K., and G. Tsinidis (2014). Performance and seismic design of underground structures, in *Earthquake Geotechnical Engineering Design*, M. Maugeri and C. Soccodato (Editors), Springer, 279–340, doi: 10.1007/978-3-319-03182-8\_11.
- Sager, K., L. Ermert, C. Boehm, and A. Fichtner (2018). Towards full waveform ambient noise inversion, *Geophys. J. Int.* **212**, no. 1, 566–590.
- Shapiro, N. M., M. Campillo, L. Stehly, and M. H. Ritzwoller (2005). High-resolution surface-wave tomography from ambient seismic noise, *Science* 307, no. 5715, 1615–1618.
- Snieder, R. (2004). Extracting the Green's function from the correlation of coda waves: A derivation based on stationary phase, *Phys. Rev. E* **69**, no. 4, 046,610.
- Tanimoto, T. (2007). Excitation of microseisms, *Geophys. Res. Lett.* **34**, no. 5, doi: 10.1029/2006GL029046.
- Tanimoto, T., C.-J. Lin, C. Hadziioannou, H. Igel, and F. Vernon (2016). Estimate of Rayleigh-to-Love wave ratio in the secondary microseism by a small array at Pinon flat observatory, California, *Geophys. Res. Lett.* 43, no. 21, 11–173.
- Tarantola, A. (2005). *Inverse Problem Theory and Methods for Model Parameter Estimation*, SIAM, doi: 10.1137/1.9780898717921.
- Williams, E. F., M. R. Fernández-Ruiz, R. Magalhaes, R. Vanthillo, Z. Zhan, M. González-Herráez, and H. F. Martins (2019). Distributed sensing of microseisms and teleseisms with submarine dark fibers, *Nat. Commun.* **10**, no. 1, 1–11.
- Williams, E. F., M. R. Fernández-Ruiz, R. Magalhaes, R. Vanthillo, Z. Zhan, M. González-Herráez, and H. F. Martins (2021). Scholte wave inversion and passive source imaging with ocean bottom DAS, *The Leading Edge* 40, no. 8, 576–583.
- Yang, Y., J. W. Atterholt, Z. Shen, J. B. Muir, E. F. Williams, and Z. Zhan (2022). Sub-kilometer correlation between near-surface structure and ground motion measured with distributed acoustic sensing, *Geophys. Res. Lett.* 49, no. 1, e2021GL096503, doi: 10.1029/2021GL096503.
- Yang, Y., Z. Zhan, Z. Shen, and J. Atterholt (2022). Fault zone imaging with distributed acoustic sensing: Surface-to-surface wave scattering, J. Geophys. Res. e2022JB024329, doi: 10.1029/2022JB024329.
- Zhan, Z. (2020). Distributed acoustic sensing turns fiber-optic cables into sensitive seismic antennas, *Seismol. Res. Lett.* **91**, no. 1, 1–15.

Manuscript received 18 July 2022 Published online 2 November 2022